

## BLAZAR SPECTRA WITH HARD-SPHERE-LIKE ACCELERATION OF ELECTRONS

KATSUAKI ASANO<sup>1</sup>, AND MASAOKI HAYASHIDA<sup>2</sup>

<sup>1</sup>Institute for Cosmic Ray Research, The University of Tokyo, 5-1-5 Kashiwanoha, Kashiwa, Chiba 277-8582, Japan;  
asanok@icrr.u-tokyo.ac.jp and

<sup>2</sup>Department of Physics, Faculty of Science and Engineering, Konan University, 8-9-1 Okamoto, Kobe, Hyogo 658-8501, Japan;  
mahaya@center.konan-u.ac.jp

*Draft version May 28, 2018*

### ABSTRACT

Electrons emitting non-thermal photons in blazars are possibly accelerated by turbulences developed in jets. In this paper, we consider the case so-called hard-sphere scattering as an interaction model between turbulences and electrons, in which the acceleration timescale is independent of the electron energy. We numerically simulate broad-band emission from blazar jets with a one-zone time-dependent code, taking into account the turbulence acceleration. Our model reproduces various blazar spectra with simple assumptions, such as constant particle injection rate, constant diffusion coefficient, and conical geometry of the jet. We also discuss possible mechanism to realize the hard-sphere-like acceleration in blazar jets.

*Subject headings:* acceleration of particles — quasars: individual (Mrk 421, 1ES 1959+650, PKS 2155-304, 3C 279, PKS 1510-089) — radiation mechanisms: non-thermal — turbulence

### 1. INTRODUCTION

The double-peak structure of blazar spectra is well modeled with leptonic models (e.g. Ghisellini et al. 1985; Dermer & Schlickeiser 1993; Sikora et al. 1994; Tavecchio et al. 1998; Böttcher & Bloom 2000; Kino et al. 2002; Celotti & Ghisellini 2008; Böttcher et al. 2013). In the leptonic models, gamma-ray emission is generated via inverse Compton (IC) scattering. The synchrotron-self Compton (SSC) process up-scatters synchrotron photons produced by the same electron population in jets (e.g. Maraschi et al. 1992). Since Flat Spectrum Radio Quasars (FSRQs) have more luminous disk, external photons surrounding the disk dominate the seed photons for the IC scattering (e.g. Sikora et al. 1994). In most models, the non-thermal electrons are assumed to be accelerated via shocks with the Fermi process. However, there are several unsolved problems in the particle acceleration mechanism in blazars. Some blazar spectra imply that the electron power-law index is smaller than 2, the value from the simplest shock acceleration model. The change of the index at the spectral break is very large inconsistently with the cooling break (see e.g. Hayashida et al. 2012; Yan et al. 2014). To reproduce the curved photon spectra, an emission model requires an electron energy distribution with many phenomenological parameters, such as a double-broken power-law with a low-energy cutoff (e.g. Abdo et al. 2011).

The maximum electron energy in blazars is much smaller than the value implied from the Bohm limit (Inoue & Takahara 1996). The acceleration timescale in blazars seems to be very long compared to the timescale of the shock acceleration considered in supernova remnants (Aharonian & Atoyan 1999) or pulsar wind nebulae (Atoyan & Aharonian 1996).

Also from the theoretical point of view, the shock acceleration in blazars has difficulties. To dissipate significant kinetic energy consistently with blazar luminosity, a relativistic shock is favored. However, a relativistic

shock tends to become superluminal (Kirk & Heavens 1989), where electrons moving along the magnetic field in the downstream cannot return to the upstream so that the shock acceleration is inhibited (Sironi et al. 2015). Furthermore, the shock acceleration can operate only in weakly magnetized plasma (Lemoine & Pelletier 2011), which may contradict the magnetization implied from the spectral modeling (e.g. Tavecchio et al. 1998; Hayashida et al. 2015). This is because, for a relativistic shocks propagating in a marginally magnetized plasma, the turbulence in the upstream as the shock precursor is hard to be excited by the particles reflected from the shock front. The absent of the precursor turbulence in the upstream prohibits electrons from returning to the downstream.

As for the spectral hardness in the shock acceleration theory, the nonlinear effect of the cosmic-ray pressure may modify the shock structure and harden the electron spectrum (Malkov & Drury 2001). However, a Monte Carlo simulation by Ellison et al. (2013) shows that the nonlinear effect of the cosmic-ray on the shock structure weakens, and the acceleration efficiency is also suppressed, as the shock speed becomes relativistic.

An alternative candidate of acceleration mechanism is the stochastic acceleration by turbulence (e.g. Schlickeiser 1984; Park & Petrosian 1995; Becker et al. 2006; Cho & Lazarian 2006; Stawarz & Petrosian 2008), which is phenomenologically equivalent to the second-order Fermi acceleration. The required turbulence may be excited by Kelvin–Helmholtz instability (Rossi et al. 2008) at the boundary of the spine–sheath structure (Ghisellini et al. 2005), Rayleigh–Taylor and Richtmyer–Meshkov instabilities in the transverse jet structure (Matsumoto & Masada 2013), kink instability (Bromberg & Tchekhovskoy 2016), tearing mode instability (Sironi & Spitkovsky 2014), or the star–jet interaction (Barkov et al. 2012).

The turbulence acceleration is slower process than the

shock acceleration. In addition, this process can produce a hard electron spectrum with an index smaller than 2. Given the energy diffusion coefficient  $D_{\varepsilon\varepsilon} \propto \varepsilon^q$ , the number spectrum in the steady state without the escape effect is proportional to  $\varepsilon^{1-q}$ , where  $\varepsilon$  is the particle energy. If the particle scattering is dominated by the gyro-resonant scattering with turbulent waves, the power-law index  $q$  in  $D_{\varepsilon\varepsilon}$  is determined by the magnetic wave spectrum as  $\delta B^2(k) \propto k^{-q}$  (Blandford & Eichler 1987).

The turbulent acceleration model has been adopted to blazars by many authors (e.g. Böttcher et al. 1999; Schlickeiser & Dermer 2000; Kakuwa et al. 2015; Asano et al. 2014; Asano & Hayashida 2015). However, Kakuwa et al. (2015) shows that a very extreme parameter set, such as tiny emission region, is required to reproduce the spectra of Mrk 421 and Mrk 501 by the steady state one-zone model. The results in Kakuwa et al. (2015) imply that the steady state of the electron energy distribution is hard to be realized by the balance among the turbulence acceleration, injection, cooling, and escape of electrons. In the slow acceleration process, the temporal evolution of the electron energy density along the jet is essential to discuss the resultant photon spectrum. Adopting the Kolmogorov index ( $q = 5/3$ ), Asano et al. (2014) shows that a model taking into account the radial evolution of the electron energy distribution reconciles the observed spectrum of Mrk 421, but the model in Asano et al. (2014) requires a non-trivial evolution of the electron injection rate.

On the other hand, the model in Asano & Hayashida (2015) succeeds in reproducing the spectra for both the steady and flare states of 3C 279 with a simple assumption and the hard-sphere index  $q = 2$ , with which the acceleration timescale is independent of the particle energy.

In this paper, we pursue the hard-sphere-like acceleration in blazars by fitting spectra of five representative blazars, Mrk 421, 1ES 1959+650, PKS 2155-304, 3C 279 and PKS 1510-080, taking into account the radial evolution of the electron energy distribution. The sample consists of both types of blazars, BL Lac objects and FSRQs. Blazars emission often shows strong variability. Thanks to recent improvements of observational instruments, broad-band data from contemporaneous observations become available not only in high-flux flaring states but also in general steady states of the blazars. We demonstrate that the broad-band spectra of those blazars in the steady states are reproduced with the hard-sphere-like acceleration model with a small number of parameters.

In §2, we explain our model and method to produce model spectra. The results for several blazars are summarized in §3. §4 is devoted to discuss the implication for the acceleration mechanism in blazars.

## 2. METHOD

In this paper, the steady state photon spectrum is calculated by the numerical code in Asano et al. (2014) (see also, Asano & Hayashida 2015). To explain the model parameters summarized in Table 1, we shortly review the calculation method below. The steady emission from a blazar is modeled with a steady outflowing jet, for which we consider continuous shell ejection from the initial radius  $R_0$ . Although a conical jet with an opening angle of

$1/\Gamma$  is assumed to calculate the emission, where  $\Gamma$  is the bulk Lorentz factor of the jet, the electron injection rate  $\dot{N}'$  is normalized by a spherically-equivalent volume,

$$V'_0 = 4\pi R_0^3/\Gamma, \quad (1)$$

at  $R = R_0$ . Hereafter, we denote values in the comoving frame by prime characters. The volume expands as  $V' \propto R^2$  for the conical geometry. The electron injection rate into the above reference volume  $\dot{N}'$  is assumed as constant during the expansion timescale. Then, the injection rate density behaves as  $\dot{n}' = \dot{N}'/V' \propto R^{-2}$  from  $R = R_0$  to  $2R_0$ . The electron injection is monoenergetic with an initial Lorentz factor of  $\gamma'_{\text{inj}}$ . We have confirmed that a power-law injection yields a harder electron spectrum than the examples in this paper. Since our purpose is to yield a soft spectrum with the turbulence acceleration model, we assume the monoenergetic injection.

The particle acceleration by turbulences is regulated by the energy diffusion coefficient,

$$D'_{\varepsilon\varepsilon} = K\varepsilon_e'^2, \quad (2)$$

where  $\varepsilon_e'$  is the electron energy. In this paper, we consider only the hard-sphere type acceleration as defined in equation (2). The parameter  $K$  is constant for  $R \leq 2R_0$ .

The radial evolution of the electron energy distribution is calculated taking into account the electron injection, turbulence acceleration, radiative cooling, and adiabatic cooling. For  $R > 2R_0$  the injection and energy diffusion shut down. Our numerical code follows the evolution of the electron energy distribution and photon production as far as  $R = R_{\text{out}}$ . The synchrotron emissivity and self-absorption are calculated with the magnetic field evolving as

$$B' = B_0 \left( \frac{R}{R_0} \right)^{-1}, \quad (3)$$

where  $B_0$  is the initial value.

In addition to SSC, IC emission due to the external photon field (EIC) is calculated for FSRQs. The models for the external photon fields are the same as discussed in Hayashida et al. (2012) with the broad line emission and the infrared dust emission. When the broad line region (BLR) is considered as the external photon source, the energy density is written as

$$U'_{\text{UV}} = \frac{0.1\Gamma^2 L_D}{3\pi c R_{\text{BLR}}^2 (1 + (R/R_{\text{BLR}})^3)}, \quad (4)$$

where  $L_D$  is the disk luminosity, and the size of BLR is described as

$$R_{\text{BLR}} = 0.1 \left( \frac{L_D}{10^{46} \text{ erg s}^{-1}} \right)^{1/2} \text{ pc}. \quad (5)$$

The external photon spectrum from BLR is approximated by the diluted Planck distribution with photon temperature of

$$T'_{\text{UV}} = 10\Gamma \text{ eV}. \quad (6)$$

The infrared dust emission is an alternative source of the external photon field for a relatively larger  $R_0$ . In

this case, we adopt a steeply dropping function as

$$U'_{\text{IR}} = \frac{0.1\Gamma^2 L_D}{3\pi c R_{\text{IR}}^2 (1 + (R/R_{\text{IR}})^4)}. \quad (7)$$

The parameters in this case are expressed as

$$R_{\text{IR}} = 2.5 \left( \frac{L_D}{10^{46} \text{ erg s}^{-1}} \right)^{1/2} \text{ pc}, \quad (8)$$

$$T'_{\text{IR}} = 0.3\Gamma \text{ eV}. \quad (9)$$

In summary, the model parameters are  $\Gamma$ ,  $R_0$ ,  $B_0$ ,  $\gamma'_{\text{inj}}$ ,  $K$ ,  $R_{\text{out}}$ , and  $L_D$ . The shape of the electron spectrum is adjusted by only the diffusion coefficient  $K$  and the cooling effect. The conically expanding outflow in this model seems reasonable and simplest assumption. We do not need to put an additional parameter for particle escape. The adiabatic cooling effect suppresses the emission at  $R \gg R_0$ , so that the steady outflow results in a steady emission without the escape effect.

### 3. RESULTS

We select several spectral data for the blazars in non-flaring states. The model parameters we obtained are summarized in Table 1. In all the cases, the acceleration timescale  $K^{-1}$  is comparable to the dynamical timescale  $R_0/(\Gamma c)$ . A slight difference in  $K$  results in a drastic change of the resultant photon spectrum. Below we discuss the individual cases.

#### 3.1. Mrk 421

First, we discuss a famous BL Lac object Mrk 421 (redshift  $z = 0.031$ ) based on the spectrum of the 4.5 month long multifrequency campaign (Abdo et al. 2011). For this data set, Asano et al. (2014) and Kakuwa et al. (2015) have already fitted the spectrum with turbulence acceleration models. The steady one-zone model of Kakuwa et al. (2015) requires a nontrivial energy-dependence of the diffusion coefficient,  $D'_{\epsilon\epsilon} \propto \epsilon_e^{1.85}$ , and very small region ( $\sim 10^{14}$  cm) to make electrons escape faster. On the other hand, the model in Asano et al. (2014) is the same as the model in this paper, but the diffusion coefficient was assumed as the Kolmogorov type,  $D'_{\epsilon\epsilon} \propto \epsilon_e^{5/3}$ . To reproduce the broad photon spectrum, a rapid evolution of the particle injection with radius was required. In this section, we demonstrate that the hard-sphere model can reproduce the spectrum even with a constant injection rate. The macroscopic parameters  $R_0$  and  $\Gamma$  in our model roughly agree with the values in the original work on the campaign data (Abdo et al. 2011). The variability timescale  $\sim R_0/\Gamma^2$  corresponds to about 0.3 day.

Figure 1 shows the radial evolution of the electron energy distribution for model A (see Table 1). Here, we inject electrons with the initial Lorentz factor  $\gamma'_{\text{inj}} = 10$ . In the hard-sphere case, the electron energy distribution is sensitive to the ratio of the acceleration timescale  $K^{-1}$  to the elapsed time  $t'$  as analytically demonstrated in Asano & Mészáros (2016). The energy injected from turbulence grows exponentially as  $\propto \exp(Kt')$  for  $Kt' \geq 1$ . In the low-energy part above  $\gamma'_{\text{inj}} m_e c^2$ , the spectrum can be approximated as a power-law of  $n'(\epsilon'_e) \propto \epsilon'_e{}^{-1}$ . The spectral shape around the peak is curved, which

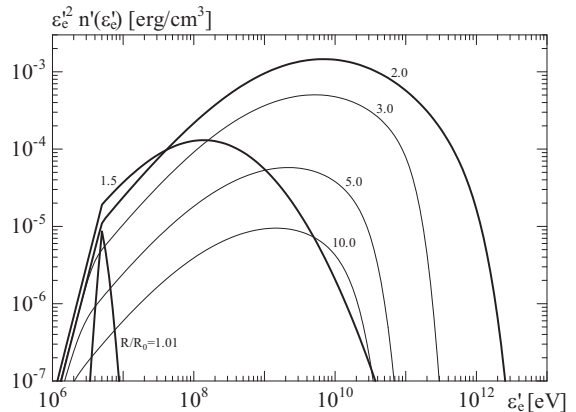


FIG. 1.— Evolutions of the energy distribution of the electron density in the model A for Mrk 421.

is characteristic for the stochastic acceleration. After the shutdown of the electron acceleration and injection ( $R > 2R_0$ ), we can see that the adiabatic cooling effect shifts the spectral shape to lower energy.

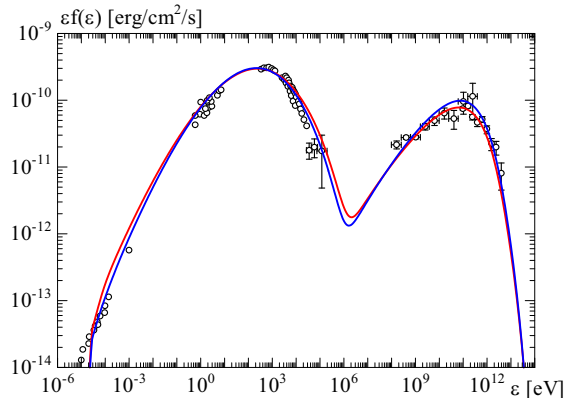


FIG. 2.— Model photon spectra A (red) and B (blue) for Mrk 421. The observed data points are partially extracted from the data of the 4.5 month campaign (Abdo et al. 2011).

Owing to the curved electron spectrum and its radial evolution, the curved spectrum for Mrk 421 is well reproduced even from radio to gamma-ray as shown by the red line in Figure 2. The synchrotron spectrum is broad enough to agree with the observation differently from the Kolmogorov case in Asano et al. (2014). Although the radio data seems on the extrapolation from the optical/IR data, the radio emission has been neglected as another component in the previous models (e.g., Tramacere et al. 2009; Abdo et al. 2011), in which absorption due to synchrotron self-absorption is crucial in the radio band. Owing to the hard electron spectrum in our model, the emission region is optically thin even for radio emission.

Here, we also test model B (blue), in which  $\gamma'_{\text{inj}}$  is higher. Even for a different value of  $\gamma'_{\text{inj}}$ , which is highly uncertain, a slight change of the other parameters produces a quite similar spectrum. As shown in Figure 2, a higher  $\gamma'_{\text{inj}}$  tends to produce a slightly narrower spectrum.

#### 3.2. 1ES 1959+650

TABLE 1  
 MODEL PARAMETERS

		$\gamma'_{\text{inj}}$	$R_0$ cm	$R_{\text{out}}/R_0$	$\Gamma$	$B_0$ G	$K$ $\text{s}^{-1}$	$\dot{N}'$ $\text{s}^{-1}$	$L_D$ $\text{erg s}^{-1}$	UV/IR
Mrk 421	A	10	$1.5 \times 10^{17}$	30	15	0.18	$4.8 \times 10^{-6}$	$2.4 \times 10^{47}$	—	—
	B	100	$1.5 \times 10^{17}$	30	15	0.16	$3.7 \times 10^{-6}$	$9.8 \times 10^{46}$	—	—
1ES 1959+650	A	100	$1.6 \times 10^{17}$	30	20	0.18	$5.0 \times 10^{-6}$	$3.7 \times 10^{46}$	—	—
	B	100	$1.6 \times 10^{17}$	10	20	0.18	$5.0 \times 10^{-6}$	$3.7 \times 10^{46}$	—	—
	C	10	$4.0 \times 10^{16}$	30	40	0.5	$4.3 \times 10^{-5}$	$1.5 \times 10^{47}$	—	—
PKS 2155–304		10	$6.0 \times 10^{16}$	30	20	1.2	$1.2 \times 10^{-5}$	$1.5 \times 10^{48}$	—	—
3C 279		10	$7.1 \times 10^{16}$	30	15	8.0	$9.5 \times 10^{-6}$	$7.3 \times 10^{49}$	$6.0 \times 10^{45}$	UV
PKS 1510–089		10	$6.0 \times 10^{17}$	30	20	0.38	$9.0 \times 10^{-7}$	$7.3 \times 10^{49}$	$5.0 \times 10^{45}$	IR

1ES 1959+650 ( $z = 0.047$ ) is categorized as a high-frequency peaked BL Lac object (HBL) and one of the most frequently observed TeV gamma-ray blazars. Here we focus on a multi-wavelength campaign conducted during a low TeV flux state in May 2006, where simultaneous X-ray data by Suzaku and very-high-energy gamma-ray data by MAGIC are available (Tagliaferri et al. 2008).

As shown in Figure 3, the synchrotron component shows a similar shape to that in Mrk 421. Compared to the spectrum of Mrk421, the spectral peak energies of the synchrotron and SSC components are similar while the ratio of the gamma-ray flux to the synchrotron flux in 1ES 1959+650 is relatively small. It suggests that the typical electron energy and magnetic field may be similar in the two objects, but the efficiency of the SSC emission in 1ES1959+650 needs to be reduced by increasing the bulk Lorentz factor slightly.

Our results are summarized in Figure 3, in which the parameter values of  $R_0$ ,  $\Gamma$ , and  $B_0$  are basically consistent with the previous results in Tagliaferri et al. (2008). Model A (red) approximately reproduces the curved spectral shape for the synchrotron component, but the IR/optical flux is slightly higher than the observed flux. This difference may be within theoretical uncertainty in our idealized model. For instance, since the magnetic field may be not purely toroidal, the field may decay faster than  $B' \propto R^{-1}$ . In such a case, the synchrotron emission for a large  $R$  would be suppressed. As model B (blue, where  $R_{\text{out}} = 10R_0$ ) shows, if the emission from  $R > 10R_0$  is neglected, the synchrotron spectrum becomes more consistent with the observed data. The slight difference in the spectra below 10 eV between models A and B exhibits the small contribution of emission at  $R > 10R_0$ .

While the spectral shape of the synchrotron component in model A or B seems consistent with the observation, the gamma-ray spectrum may contradict the observed data in the GeV energy range. Note that the gray data points in the GeV range shown in Figure 3 are 4-year averaged spectral data, and they were not simultaneously obtained with the data in other energy ranges. The variability in the GeV energy range (e.g., Kaur et al. 2017; Patel et al. 2018) may resolve the discrepancy. If we seriously incorporate the soft spectrum indicated by the *Fermi* data points, a broader energy distribution is required for electrons. Model C (green), in which a smaller  $\gamma'_{\text{inj}}$  and higher  $\Gamma$  are adopted, shows a broader gamma-ray spectrum. Even in this case, the

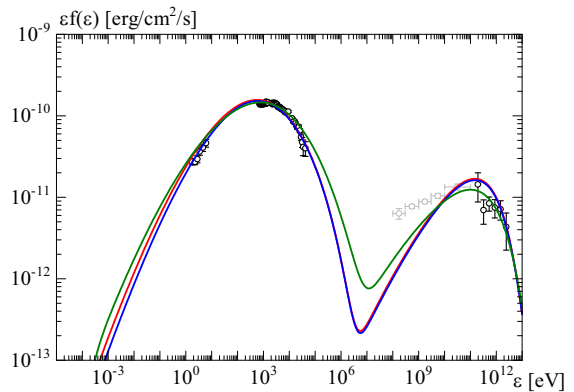


FIG. 3.— Model photon spectra A (red), B (blue) and C (green) for 1ES 1959+650. The black open circles are measured flux points from the multiwavelength campaign in 2006 May (Tagliaferri et al. 2008). The gray open circles are taken from the LAT 4-year Point Source Catalog (3FGL, Acero et al. 2015).

model flux below 1 GeV is significantly lower than the observed data, and the synchrotron spectrum becomes broader than the data. To reconcile both the narrow synchrotron and soft IC component, an external photon field may be required as discussed in Asano et al. (2014).

### 3.3. PKS 2155–304

PKS 2155–304 ( $z = 0.116$ ) is one of the most luminous HBL objects in the TeV energy band. The object is famous for short-timescale variability ( $\sim$  minutes) in the TeV gamma-rays. Recently, a spectral hardening in the hard X-ray band has been discovered from observations with the NuSTAR satellite (Madejski et al. 2016). The spectral hardening can be interpreted by the onset of the IC component. The observations were performed in a very low X-ray state together with XMM-Newton and Swift-UVOT, which provide soft X-ray and UV data for the synchrotron component. We apply our model for the broad band spectrum also including gamma-ray data by *Fermi*-LAT as reported in Madejski et al. (2016).

As the thin grey line in Figure 4 shows, the photon spectrum is fitted by a model with a broken power-law electron distribution (the low-energy index is 2.2, high-energy index is 3.8, and the break Lorentz factor is  $2.6 \times 10^4$ ) in Madejski et al. (2016). However, this soft electron spectrum implies the proton luminosity of  $> 10^{47} \text{ erg s}^{-1}$  assuming the same number for protons and electrons. Madejski et al. (2016) concluded that the obtained proton luminosity is too large as an HBL-type blazar.

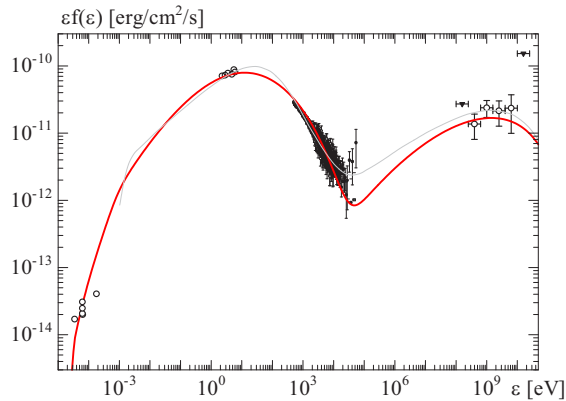


FIG. 4.— Model photon spectrum (red) for PKS 2155–304. The open circles for optical, X-ray and gamma-ray are fluxes measured in 2013 April (Madejski et al. 2016). The gray thin line is the broken power-law model in Madejski et al. (2016). The radio data points represent core fluxes taken from NASA/IPAC Extragalactic Database (NED)

The hard spectrum in the turbulence acceleration model significantly suppresses the number of electrons. The model shown in Figure 4 (red) seems consistent with the curved feature in the soft X-ray data. In this model, the mean energy of electrons is about GeV: the mean Lorentz factor is  $\sim 2000$ , while that is 5.6 in the model of Madejski et al. (2016). Thus, we can reduce the proton luminosity by a factor of 400.

However, the model flux in the hard X-ray regime is lower than the best-fit model of Madejski et al. (2016), because our model spectrum is significantly harder than the model in Madejski et al. (2016). To reconcile with the hard X-ray flux, we need another external photon field as the IC seed photons again (see the model and discussion in Asano et al. 2014).

#### 3.4. 3C 279

We revisit a famous FSRQ 3C 279 ( $z = 0.538$ ), while we have tested this blazar with the turbulence acceleration model in Asano & Hayashida (2015). The adopted data of the spectrum were obtained in an active period (period “D” in Hayashida et al. 2012), but the data are averaged over five days, which may be significantly longer than the variability timescale. Thus, we adopt a steady emission model even in this case. In Asano & Hayashida (2015), the external photon field was assumed to be spatially constant. With the photon field model explained in section 2, a similar result to Asano & Hayashida (2015) is obtained as shown in Figure 5.

The low-energy cutoff in the radio band is due to synchrotron self-absorption. The X-ray bump is attributed to SSC emission, while EIC emission produces the gamma-ray peak. The synchrotron spectral shape especially for the high-energy region is well reproduced by our model.

#### 3.5. PKS 1510–089

To test the case of the infrared dust emission as the external photon field, we fit the spectrum of a FSRQ PKS 1510–089 ( $z=0.36$ ). Nalewajko et al. (2012) obtained broad band spectra from multi-wavelength observations including Herschel satellite pointing for far-infrared bands using PACS and SPIRE instruments.

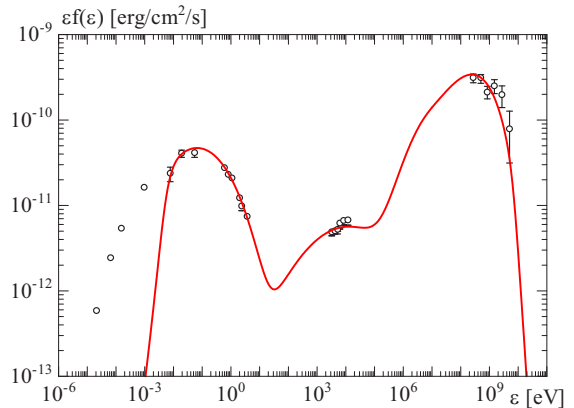


FIG. 5.— Model photon spectrum for 3C 279. The open circles are measured flux points in 2009 February (Hayashida et al. 2012).

They considered three components for the emission origin: jet emissions in BLR and the hot-dust region, and emission attributed to the accretion disk. The optical/UV bump and X-ray components are considered to be the contributions from the accretion disk and the hot disk corona, respectively, while synchrotron emission is dominant in the far-infrared band observed by Herschel.

Nalewajko et al. (2012) adopted the two zone model, where the GeV emissions are emitted from BLR and the emission from the hot-dust region does not contribute to the gamma-ray emission so much. However, Aleksić et al. (2014) reported detections of sub-TeV emission even during steady states and possible correlations between GeV gamma-ray flares and radio core appearances. Those results suggest that the gamma-ray emission is likely to be originated outside of BLR. In this paper, we consider the emission from only the hot-dust region; the X-ray and optical components are not weighted so much because of the contributions from disk and corona emission.

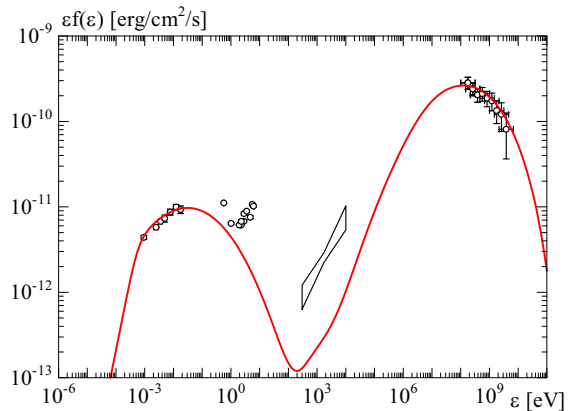


FIG. 6.— Model photon spectrum for PKS 1510–089. The open circles are measured flux points in 2011 August (epoch “H2”, Nalewajko et al. 2012).

Our model parameters in Table 1 imply that the radius  $R_0 \sim 0.2$  pc is outside  $R_{\text{BLR}} \sim 0.07$  pc, but inside the hot-dust region ( $R_{\text{IR}} \sim 1.8$  pc). Figure 6 shows our fitting results. The gamma-ray spectral component is the EIC emission from the hot-dust region. The SSC emission is negligible because of the low synchrotron photon density at the large initial radius. The success in Figure

6 suggests possible turbulence acceleration even in the hot-dust region.

#### 4. DISCUSSION

The model with the hard-sphere like electron acceleration in this paper is constructed only under simple assumptions; constant energy diffusion coefficient, constant injection rate of electrons, conical geometry ( $V' \propto R^2$ ), and  $B' \propto R^{-1}$ . Nevertheless, our model spectra have well reproduced the curved photon spectra of the blazars from the radio to the high-energy gamma-ray bands, though the low-energy tails of the SSC components for 1ES 1959+650 and PKS 2155-304 would require some modification in our model, such as an extra photon field or a low-energy extra population of electrons. In our model, the electron energy distribution is controlled by the three timescales: dynamical ( $R_0/\Gamma/c$ ), acceleration ( $1/K$ ), and cooling timescales. The combinations of those parameters can produce variety of the spectral shape without extra parameters.

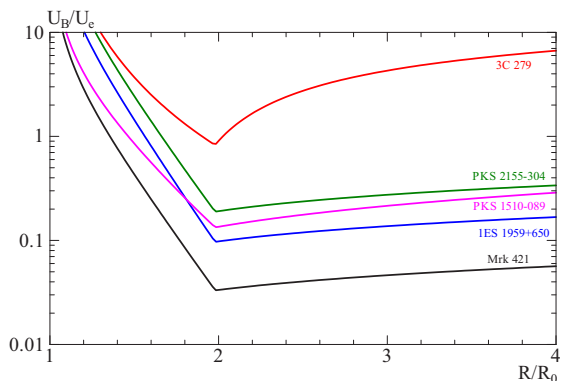


FIG. 7.— Radial evolution of the energy density ratios for model B of Mrk 421 (black), model B of 1ES 1959+650 (blue), PKS 2155-304 (green), 3C 279 (red), and PKS 1510-089 (magenta).

Here we have not specified the mechanism of the turbulence excitation to accelerate particles. One candidate is magnetic reconnection in highly magnetized plasma (e.g. Sironi & Spitkovsky 2014; Sironi et al. 2015; Oishi et al. 2015; Takamoto 2018). As Sironi et al. (2015) demonstrated numerically, the energy dissipation due to magnetic reconnection leads to an equi-partition between the magnetic field and non-thermal particles. As shown in Figure 7, the energy densities of the magnetic field and electrons are equi-partition only for the case in 3C 279 (see also, Dermer et al. 2014). In this case, magnetic reconnection is a promising mechanism for the turbulence excitation, or reconnection may directly accelerate electrons, which can be equivalent to the stochastic acceleration expressed by the diffusion coefficient in this paper.

On the other hand, the other objects in Figure 7, the magnetic field is subdominant compared to the electron energy density. Even for the case of 3C 279, it is reported that the magnetic field energy became much lower than the electron energy for the gamma-ray flare states (Hayashida et al. 2015; Asano & Hayashida 2015). In those cases, magnetic reconnection is unlikely as the energy source of turbulences or non-thermal electrons.

The acceleration timescale in the hard-sphere model

does not depend on electron energy. When particle scattering is dominated by a certain size of eddy, the acceleration timescale will be common irrespectively of electron energy. However, the turbulence may be expressed by a superposition of MHD waves in small scales.

The fast mode is the most likely dominant wave mode as the electron energy source in low-magnetized plasma implied from our results. The energy of the turbulence is injected at a large scale ( $< R_0/\Gamma$ ) as fast waves, and cascade to shorter scales following the Kolmogorov law;  $kE(k) \propto k^{-2/3}$ , where  $k$  is the wave number. On the other hand, the power spectrum of the magnetic field tends to be flatter than the kinetic one (Cho & Vishniac 2000; Cho et al. 2009). At a scale, where the magnetic power is comparable to the kinetic one, the kinetic energy transfer mechanism in the turbulence cascade process changes from the hydrodynamical one to the magnetohydrodynamic one. The power spectra for both the kinetic and magnetic energies become steeper at this equi-partition scale ( $k = k_{\max}$ , Goldreich & Sridhar 1995; Inoue et al. 2011). In this case, the acceleration timescale may be regulated by this scale.

If the Larmor radius of electrons is significantly shorter than the wavelength  $k_{\max}^{-1}$ , the pitch angle diffusion via gyro resonance is not responsible for particle scattering. In this case, the main mechanism of the energy exchange between electrons and waves is transit time damping (TTD, Berger et al. 1958); electrons are accelerated when their velocity along the magnetic field equals to the parallel component of the phase velocity. For non-relativistic waves, the number fraction of relativistic electrons that satisfy the TTD resonance condition is small. Only electrons with their pitch angle  $\sim \pi/2$  can interact with waves. However, the phase velocity of the wave in the blazar emission region may be mildly relativistic. Furthermore, the mirror force can broaden the resonance condition of TTD as shown by Yan & Lazarian (2008). We can expect that a significant fraction of electrons interact with the waves.

When electrons are scattered by waves, whose wavelength are longer than the gyro radius, the description of the second order Fermi acceleration may be valid. The scattering time scale is  $\sim (ck_{\max})^{-1}$ , and the average energy change per scattering is  $\Delta\epsilon_e/\epsilon_e \sim v(k_{\max})/c$ . Let us assume that the turbulence velocity  $v(k_{\max})$  at  $k = k_{\max}$  is expressed by the Kolmogorov law as  $v^2(k_{\max}) = v_0^2(k_{\max}/k_{\min})^{-2/3}$ , where  $v_0$  is the turbulence velocity at the injection scale  $k_{\min}^{-1}$ . Then, the acceleration frequency becomes

$$t_{\text{acc}}^{-1} \sim ck_{\max} \left( \frac{v(k_{\max})}{c} \right)^2 = ck_{\max} \left( \frac{v_0}{c} \right)^2 \left( \frac{k_{\max}}{k_{\min}} \right)^{-2/3} \quad (10)$$

Here we take model B for Mrk 421 as an example. As shown in Figure 1, TeV is sufficient for the maximum energy of electrons to reproduce the photon spectrum. In this model, the Larmor radius of TeV electrons is  $2 \times 10^{10}$  cm, which should be shorter than  $k_{\max}^{-1}$  to realize the non-gyro-resonant scattering as dominant acceleration process. On the other hand, we need a  $k_{\min}^{-1}$  shorter than  $R_0/\Gamma = 10^{16}$  cm. Those conditions imply  $k_{\max}/k_{\min} < 4.8 \times 10^5$ . With a conservative assumption of  $k_{\min} = \Gamma/R_0$ ,  $ck_{\max}(k_{\max}/k_{\min})^{-2/3} < 2.3 \times 10^{-4} \text{ s}^{-1}$ .

The turbulence velocity at the injection would be slower than the sound speed in relativistic plasma:  $(v_0/c)^2 < 1/3$ . Finally, the maximum value of  $t_{\text{acc}}^{-1}$  is estimated as  $7.8 \times 10^{-5} \text{ s}^{-1}$ , which is much larger than  $K \sim 10^{-6} \text{ s}^{-1}$  required in the model. If the turbulence is excited by the star-jet interaction, a value of  $k_{\text{min}}$  much larger than  $\Gamma/R_0$  is possible, which further shortens  $t_{\text{acc}}$ . Thus, the non-gyro-resonant scattering may provide a mechanism to realize the hard-sphere-like acceleration in blazars as required by our models.

Our simplest model with the Kolmogorov-like model ( $q = 5/3$ ) cannot fit the blazar spectra. Both the synchrotron and IC components become narrower than the observed shape for those cases. If the particle acceleration is due to turbulence in the jet, the hard-sphere-like diffusion in the energy space seems necessary. However, it is difficult to distinguish observationally turbulence acceleration from other mechanisms. As demonstrated in

Asano et al. (2014), the flare light curves may provide a hint for the acceleration mechanism. In this context, the GeV flare with a very hard spectrum in 2013 is an encouraging example as discussed in Asano & Hayashida (2015). Future gamma-ray observations including CTA will give us opportunity to verify the acceleration mechanism.

First we appreciate the anonymous referee for the helpful advice. We thank Greg Madejski and Krzysztof Nalewajko for their providing SED data points of PKS 2155-304 and PKS 1510-089. This work is supported by Grants-in-Aid for Scientific Research nos. 16K05291 (K.A.) and 18K03665 (M.H.) from the Ministry of Education, Culture, Sports, Science and Technology (MEXT) of Japan.

## REFERENCES

- Abdo, A. A., Ackermann, M., Ajello, M., et al. 2011, *ApJ*, 736, 131
- Acerro, F., Ackermann, M., Ajello, M., et al. 2015, *ApJS*, 218, 23
- Aharonian, F., Akhperjanian, A. G., Bazer-Bachi, A. R., et al. 2007, *ApJ*, 664, L71
- Aharonian, F. A., & Atoyan, A. M. 1999, *A&A*, 351, 330
- Aleksić, J., Ansoldi, S., Antonelli, L. A., et al. 2014, *A&A*, 569, A46
- Asano, K., & Hayashida, M. 2015, *ApJ*, 808, L18
- Asano, K., & Mészáros, P. 2016, *Phys. Rev. D*, 94, 023005
- Asano, K., Takahara, F., Kusunose, M., Toma, K., & Kakuwa, J. 2014, *ApJ*, 780, 64
- Atoyan, A. M., & Aharonian, F. A. 1996, *MNRAS*, 278, 525
- Barkov, M. V., Aharonian, F. A., Bogovalov, S. V., Kelner, S. R., & Khangulyan, D. 2012, *ApJ*, 749, 119
- Becker, P. A., Le, T., & Dermer, C. D. 2006, *ApJ*, 647, 539
- Berger, J. M., Newcomb, W. A., Dawson, J. M., Frieman, E. A., Kulsrud, R. M., & Lenard, A. 1958, *PhPl*, 1, 301
- Blandford, R., & Eichler, D. 1987, *PhR*, 154, 1
- Böttcher, M., & Bloom, S. D., 2000, *ApJ*, 119, 469
- Böttcher, M., Pohl, M. & Schlickeiser, R. 1999, *APh*, 10, 47
- Böttcher, M., Reimer, A., Sweeney, K., & Prakash, A. 2013, *ApJ*, 768, 54
- Bromberg, O., & Tchekhovskoy, A. 2016, *MNRAS* 456, 1739
- Celotti, A., & Ghisellini, G. 2008, *MNRAS*, 385, 283
- Cho, J., & Lazarian, A. 2006, *ApJ*, 638, 811
- Cho, J., & Vishniac, E. T. 2000, *ApJ*, 538, 217
- Cho, J., Vishniac, E. T., Beresnyak, A., Lazarian, A., & Ryu, D. 2009, *ApJ*, 693, 1449
- Dermer, C. D., Cerruti, M., Lott, B., Boisson, C., & Zech, A. 2014, *ApJ*, 782, 82
- Dermer, C. D., & Schlickeiser, R. 1993, *ApJ*, 416, 458
- Ellison, D. C., Warren, D. C., & Bykov, A. M. 2013, *ApJ*, 776, 46
- Ghisellini, G., Maraschi, L., & Treves, A. *A&A*, 146, 204
- Ghisellini G., Tavecchio F., & Chiaberge M. 2005, *A&A*, 432, 401
- Goldreich, P. & Sridhar, S., 1995, *ApJ*, 438, 763
- Hayashida, M., Madejski, G. M., Nalewajko, K., et al. 2012, *ApJ*, 754, 114
- Hayashida, M., Nalewajko, K., Madejski, G. M., et al. 2015, *ApJ*, 807, 79
- Inoue, T., Asano, K., & Ioka, K. 2011, *ApJ*, 734, 77
- Inoue, S., & Takahara, F. 1996, *ApJ*, 463, 555
- Kakuwa, J., Toma, K., Asano, K., et al. 2015, *MNRAS*, 449, 551
- Kaur, N., Chandra, S., Baliyan, K. S., et al. 2017, *ApJ*, 846, 158
- Kino, M., Takahara, F., & Kusunose, M. 2002, *ApJ*, 564, 97
- Kirk, J. G., & Heavens, A. F. 1989, *MNRAS*, 239, 995
- Lazarian, A., & Vishniac, E. T. 1999, *ApJ*, 517, 700
- Lefa, E., Rieger, F. M., & Aharonian, F. 2011, *ApJ*, 740, 64
- Lemoine, M., & Pelletier, G. 2011, *MNRAS*, 417, 1148
- Madejski, G. M., Nalewajko, K., Madsen, K. K., et al. 2016, *ApJ*, 831, 142
- Maraschi, L., Ghisellini, G., & Celotti, A. 1992, *ApJ*, 397, L5
- Matsumoto, J., & Masada, Y. 2013, *ApJ*, 772, L1
- Malkov, M. A., & Drury, L. O’C. 2001, *RPPh*, 64, 429
- Nalewajko, K., Sikora, M., Madejski, G. M., et al. 2012, *ApJ*, 760, 69
- Oishi, J. S., Mac Low, M.-M., Collins, D. C., & Tamura, M. 2015, *ApJ*, 806, L12
- Park, B., & Petrosian, V. 1995, *ApJ*, 446, 699
- Patel, S. R., Shukla, A., Chitnis, V. R., et al. 2018, *A&A*, 611, A44
- Rossi, P., Mignone, A., Bodo, G., Massaglia, S., & Ferrari, A. 2008, *A&A*, 488, 795
- Schlickeiser, R. 1984, *A&A*, 136, 227
- Schlickeiser, R., & Dermer, C. D. 2000, *A&A*, 360, 789
- Sikora, M., Begelman, M. C., & Rees, M. J. 1994, *ApJ*, 421, 153
- Sironi, L., & Spitkovsky, A. 2014, *ApJ*, 783, L21
- Sironi, L., Petropoulou, M., & Giannios, D. 2015, *MNRAS*, 450, 183
- Stawarz, L., & Petrosian, V. 2008, *ApJ*, 681, 1725
- Tavecchio, F., Maraschi, L., & Ghisellini, G. *ApJ*, 509, 608
- Tramacere, A., Giommi, P., Perri, M., Verrecchia, F., & Tosti, G. 2009, *A&A*, 501, 879
- Takamoto, M. 2018, accepted for *MNRAS*, arXiv:1802.07549
- Tagliaferri, G., Foschini, L., Ghisellini, G., et al. 2008, *ApJ*, 679, 1029
- Yan, H. & Lazarian, A. 2008, *ApJ*, 673, 942
- Yan, D., Zeng, H., & Zhang, L. 2014, *MNRAS*, 439, 2933